PNAS RESEARCH ARTICLE | ENGINEERING

Origami frustration and its influence on energy landscapes of origami assemblies

Shixi Zang[a], Tuo Zhao[a], Diego Misseroni[b,1], and Glaucio H. Paulino[a,c,1]

Affiliations are included on p. 11.

Edited by Hanqing Jiang, Westlake University, Hangzhou, China; received December 20, 2024; accepted July 21, 2025 by Editorial Board Member John A. Rogers

Harnessing instabilities of multicomponent multistable structural assemblies can potentially lead to scalable and reversible functionalities, which can be enhanced by exploring frustration. For instance, standard Kresling origami cells exhibit nontunable intrinsic energy landscapes determined by their geometry and material properties, limiting their adaptability after fabrication. To overcome this limitation, we introduce frustration to enable fine-tuning of the energy landscape and resulting deformation states. By prestressing the Kresling cell by means of special springs with individual control, we induce either global or localized (i.e., crease level) frustration, which allows changing the energy barrier (cell or assembly). We investigate the mechanical behavior of frustrated Kresling assemblies, both theoretically and experimentally, under various loading and boundary conditions. Our findings reveal that changing the frustration state leads to precise control of folding sequences, enabling previously inaccessible folding paths. The proposed concept paves the way for applications in mechanical metamaterials and other fields requiring highly programmable and reconfigurable systems – e.g., prosthetic limbs.

geometrical frustration | origami | Kresling | energy landscape

Reconfigurable assemblies consist of engineered macroscopic nonlinear structures undergoing large deformations. The behavior of the assemblies depends on the material properties and geometrical nonlinearity of the local unit cells. Classic nonlinear cells, such as snap-through beams (1, 2), and buckling-driven continuum elements(3, 4), have been explored in applications, including energy absorption (5, 6), soft robotic actuators (7, 8), noncommutative response (9), wave propagation (10), acoustic metamaterials (11, 12), and soft matter undergoing dramatic shape changes (13, 14). More recently, origami-inspired geometry has enriched the design space of the nonlinear unit cells such as Kresling (15–20), square-twist (21, 22), Waterbomb (23, 24), and Miura-Ori variations (25–27), and curved folds (28, 29). Furthermore, the nonrigid origami assemblies have enabled finite deformation for applications involving shape morphing (30–32) and controllable energy landscape (32–34). The aforementioned reconfigurable assemblies assume a predefined deformation path; thus, the nonlinear properties, e.g., the shape of the energy landscape and the instability behavior, are nontunable after fabrication. On the other hand, reprogrammable structures enable continuously variable elastic modulus via changing the configurational state of local units (35), e.g., heights of the elastic shells (36), rotation angles of the gears (37), and rolling motion of the cams (38). A limited number of studies have applied this reprogrammability concept for assemblies with tunable instability behaviors (39, 40), e.g., switch between monostable and bistable responses. The switching behavior is achieved by actuating two distinct topological states of a local unit. However, the limited local states restrict the number of global deformation paths, which makes it difficult to reprogram the energy barrier of the assembly continuously.

Here, we introduce geometrical frustration (41) into the origami-inspired assemblies, together with dedicated experimental fixtures (e.g., free-rotating and free-translating), to achieve continuous energy landscape reprogrammability. The geometrical frustration is embedded within the origami cells by means of three mechanisms: global stretch, global rotation, and crease (local) stretch (Fig. 1*A*). Each mechanism integrates shell-based origami with special spring elements, which introduce prestress into the frustrated origami cell. The prestress level of the frustrated model is continuously adjustable by controlling the spring properties, i.e., stretching/rotating direction and magnitude. The frustrated assemblies, with tunable prestresses, enable us to engineer the energy landscape of multiple stable states on the fly, thereby unlocking unprecedented folding paths that

Significance

Frustration: detrimental or desirable? Sometimes detrimental, but sometimes desirable to achieve new functionalities of nonrigid multistable origami structures. It provides the means to augment the energy landscape of such structures as it can be tailored to the features of the geometry of the origami unit cell and the frustration type. By equipping the cell with special, controllable, elastic springs, fine-tune control over energy barriers is enabled, facilitating precise folding sequences. Experiments demonstrate that activation or deactivation of the frustration can enhance the programmability of a multicell origami array, unlocking otherwise infeasible folding paths. With potential impact in fields such as mechanical computing and noncommutative state transition, this approach offers possibilities for scalable and adaptable structures with high tunability.

The authors declare no competing interest.

This article is a PNAS Direct Submission. H.J. is a guest editor invited by the Editorial Board.

[1]To whom correspondence may be addressed. Email: diego.misseroni@unitn.it or gpaulino@princeton.edu.

This article contains supporting information online at https://www.pnas.org/lookup/suppl/doi:10.1073/pnas.2426790122/-/DCSupplemental.

Published September 5, 2025.

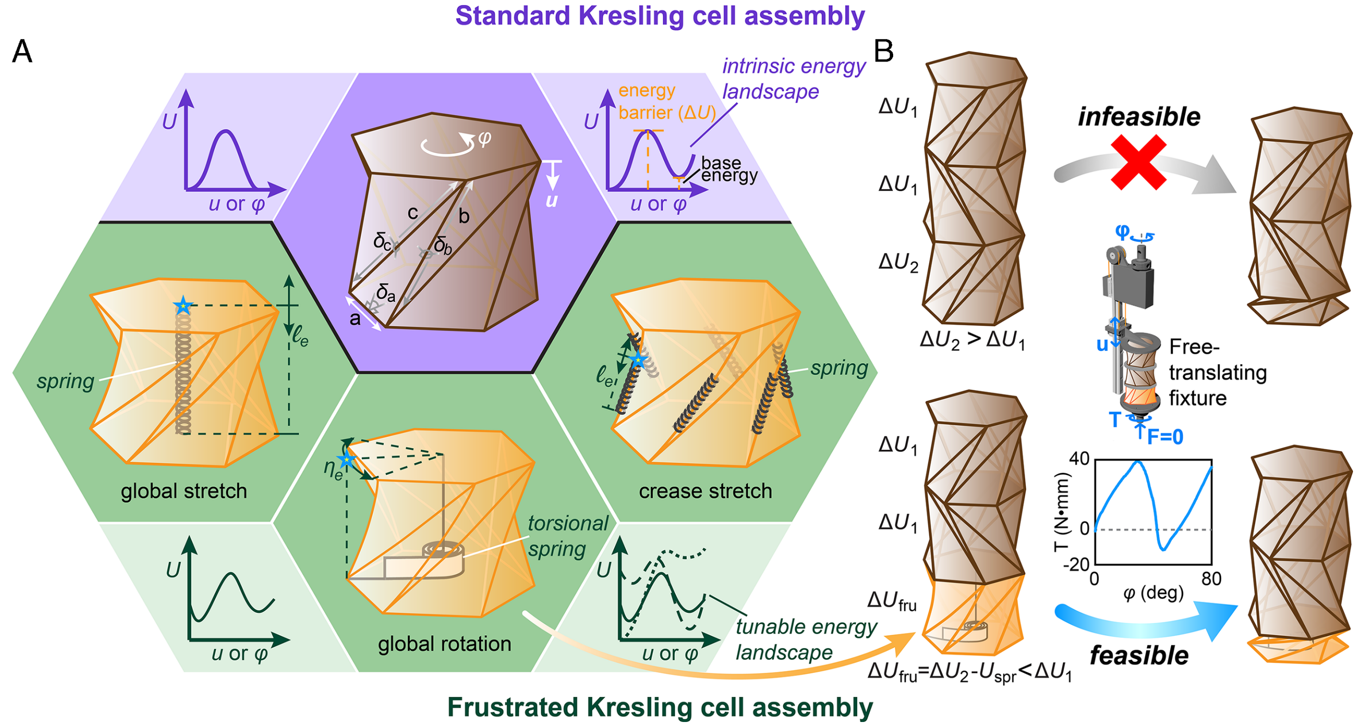

Fig. 1. Standard and geometrically frustrated origami assemblies with tunable energy landscapes and folding paths. (*A*) *Top*: Schematic of the standard Kresling origami (brown) and its intrinsic energy landscapes. The symbols u and φ denote displacement and twist angle, respectively. *Bottom*: Schematics of the frustrated models (orange) with three types of prestress: i) global stretch, ii) global rotation, and iii) crease stretch (local) and their tunable energy landscapes. The symbols ℓ_e and η_e denote the length of the axial spring and the rotating angle of the torsional spring, respectively. (*B*) *Top*: an infeasible folding path using the standard Kresling assembly. Here, ΔU_1 and ΔU_2 denote the intrinsic energy barriers of the origami cells made of different materials. *Bottom*: frustrated assembly achieving an unprecedented folding deformation. Here, ΔU_{fru} and U_{spr} denote the energy barrier of the frustrated model and the elastic energy stored in the torsional spring element, respectively. *Insets* show the rotational test setup with the free-translating fixture and experimental data of twist angle φ versus torque T.

would otherwise be infeasible (Fig. 1*B* and Movie S1). This finding paves the way for potential applications in reconfigurable mechanical metamaterials and noncommutative state transitions.

Results

Theory of Geometrical Frustration. Starting from the theoretical modeling of the Kresling origami, which describes its mechanics through an elastic energy dependent on two independent variables, displacement u and twist angle φ, we develop an enhanced model for the frustrated system. We write the total elastic energy of the frustrated model, $U_{\mathrm{fru}}(u,\varphi)$, as follows:

$$U_{\mathrm{fru}}(u,\varphi) = U_{\mathrm{spr}}(u,\varphi) + U(u,\varphi), \qquad [1]$$

where $U(u,\varphi)$ is the elastic energy of the standard Kresling cell (42), and $U_{\mathrm{spr}}(u,\varphi)$ denotes the elastic energy stored in the prestressed springs, which embed frustration into the origami cell. The five-term elastic energy of the standard cell is expressed as:

$$\begin{aligned} U(u,\varphi) = {} & \frac{1}{2} n_b k_{s,b} (b(u,\varphi) - b_0)^2 \\ & + \frac{1}{2} n_c k_{s,c} (c(u,\varphi) - c_0)^2 \\ & + \frac{1}{2} n_a k_{r,a} (\delta_a(u,\varphi) - \delta_{a0})^2 \\ & + \frac{1}{2} n_b k_{r,b} (\delta_b(u,\varphi) - \delta_{b0})^2 \\ & + \frac{1}{2} n_c k_{r,c} (\delta_c(u,\varphi) - \delta_{c0})^2. \end{aligned} \qquad [2]$$

We offer a detailed explanation of the material parameters $k_{s,i}$ ($i = b$ and c) and $k_{r,i}$ ($i = a,\ b,$ and c), the geometric parameters b, c, δ_i ($i = a,\ b,$ and c), and the parameters n_i ($i = a,\ b,$ and c) in *SI Appendix*, section 1, Fig. S1, and Table S1.

Using the principle of minimum total potential energy, the equilibrium conditions for axial and torque loading can be derived with Eq. **1**. Specifically, the axial force and torque can be calculated as follows:

$$F_{\mathrm{fru}}(u,\varphi) = \frac{\partial U_{\mathrm{spr}}(u,\varphi)}{\partial u} + \frac{\partial U(u,\varphi)}{\partial u}, \qquad [3]$$

$$T_{\mathrm{fru}}(u,\varphi) = \frac{\partial U_{\mathrm{spr}}(u,\varphi)}{\partial \varphi} + \frac{\partial U(u,\varphi)}{\partial \varphi}. \qquad [4]$$

Here, the expression of $U_{\mathrm{spr}}(u,\varphi)$ depends on the prestressed spring mechanism of interest. We present three types of frustrated models, i.e., global stretch, global rotation, and crease stretch, in the following sessions (see details of theoretical formulation in *SI Appendix*, section 1).

Global stretch. This model involves a single deformed spring element inserted in the origami and aligned with its central axis. In the theoretical analysis, the initial state of the spring can be either extended or compressed, providing the origami with tunable prestress properties. The extended spring deforms the origami cell in the folding direction, while the compressed spring stretches the unit in the deploying direction. The prestressed spring is coupled with the origami cell to achieve a new equilibrium stage, denoted as the frustrated mode. The resulting energy landscape of the frustrated mode is programmable by adjusting the elastic energy stored in the spring element, defined as follows:

$$U_{\mathrm{spr}}(u,\varphi)=\frac{1}{2}k_{s,e}(\Delta\ell_e-u)^2, \quad [5]$$

where $k_{s,e}$ and $\Delta\ell_e$ are the stiffness and length change of the spring element embedded in the frustrated Kresling cell.

Global rotation. This model takes advantage of the rotational degree of freedom of the Kresling origami and embeds torsional prestress into the unit cell. The prestress level is controlled by a torsional spring integrated with the origami cell. The spring rotates the undeformed cell and reaches a new equilibrium state with prestresses. The spring enables two types of prestresses, which are defined as positive and negative. The positive prestress rotates the cell in the same direction as its intrinsic twisting direction, while the negative prestress rotates the unit in the opposite direction. The elastic energy functional for the torsional springs is defined as follows:

$$U_{\mathrm{spr}}(u,\varphi)=\frac{1}{2}k_{r,e}(\Delta\eta_e-\varphi)^2, \quad [6]$$

where $k_{r,e}$ and $\Delta\eta_e$ are the stiffness and rotating angle change of the torsional spring integrated in the frustrated model.

Crease (local) stretch. This model embeds prestressed springs along the mountain creases (local) of the origami cell to frustrate the system. Those local spring elements deform the unit into a new stable state with a nonzero base energy. The magnitude of the base energy and energy barrier of the frustrated model are tunable by controlling the elastic energy stored in the springs, defined as follows:

$$U_{\mathrm{spr}}(u,\varphi)=\frac{1}{2}n_e k_{s,e}(b(u,\varphi)-b_0+\Delta\ell_e)^2, \quad [7]$$

where n_e is the number of the stretching springs along the mountain creases ($n_e=3$ in this paper), $b(u,\varphi)$ is the length of the mountain crease, b_0 is the initial length of the mountain crease at the undeformed state of the Kresling cell, and $\Delta\ell_e$ is the length change of the spring element.

Parametric study. The frustrated cells integrate three types of prestressed models into the standard Kresling origami. Eqs. **5**–**7** show that the elastic energy stored in the prestressed springs is controlled by its deformation. Thus, we can navigate the energy landscape by varying the length change $\Delta\ell_e$ and rotating angle change $\Delta\eta_e$ of the spring elements, respectively (Fig. 2). We refer to *SI Appendix*, Table S2 for the selection of parameters. Recall that we denote the positive prestress as deforming the origami cell in the folding direction, while the negative prestress deforms the unit in the deploying direction. Both positive and negative prestress drive the undeformed origami into new equilibrium states with nonzero base energy, and the corresponding energy landscapes are tunable. For instance, the global stretch model enables two frustrated modes: one with negative prestress and the other one with positive prestress (Fig. 2*A*). Both modes have nonzero base energy at the initial stable state; however, in the negative mode, the energy at the second stable state always increases, while for the positive mode, the base energy of the second stable state can either increase or remain unchanged depending on the given length change in the prestressed spring. Note that the base energy of the second stable state for the positive mode is similar to the base energy of the standard Kresling. This behavior is due to the frustrating setup used in the positive mode, where the elongated spring becomes invalid after returning to its original length. By contrast, the springs are always compressed in the negative mode. Thus, the resulting energy landscapes for the two modes, negative and positive, can be quite different. This finding holds for results obtained using two independent loading conditions: compression with free-rotation (Fig. 2 *B*, *Left*) and torsion with free-translation (Fig. 2 *B*, *Right*). Notably, by controlling the level of prestress in the negative mode, we can switch the instability behavior from bistable to monostable, as shown in Fig. 2*B* (*Top*: two orange curves). Another unique feature is the capability to continuously program the energy barrier of the cell with frustration. Here, the energy barrier is defined as the difference between the local maximum on the landscape and the initial base energy. Fig. 2*C* shows the theoretical energy barrier as a function of the stretching length of the prestressed spring. Moreover, the curve shows a smooth transition between the negative mode and the positive mode. This result highlights the capability of the frustrated model to achieve fine-tuned control over energy barriers.

Another frustration model we investigate is the global rotation (Fig. 2*D*), which also has two modes similar to the global stretch, i.e., negative mode and positive mode. The negative mode integrates a prestressed torsional spring rotating the origami opposite to the twisting direction of the cell while it folds. The positive mode embeds a torsional spring that rotates the origami along the same direction while the cell folds. By controlling the prestress level of the torsional spring, we can achieve nonzero base energy for the initial stable state of the cell. Further, the shape of the energy landscape can be programmed as shown in Fig. 2*E*. As a result, the global rotation-induced frustrated cell has switchable instabilities, i.e., monostable or bistable behavior. Notably, the energy barrier between the local maximum and the initial base energy can be continuously tunable as shown in Fig. 2*F*.

The last frustration model we investigate is the crease stretch shown in Fig. 2*G*. The prestressed springs are located along some mountain creases due to fabrication considerations, as shown in the later experimental validation sessions. The crease stretch has two prestressed modes, i.e., positive mode with elongated springs and negative mode with compressed springs. The two prestressed modes enable the frustrated cell with programmable energy landscapes (Fig. 2*H*). The stored elastic energy is contributed by the stretch of prestressed springs and the deformation of the origami panels and creases. The mountain creases of the Kresling cell shorten when folding is initiated, but the creases return to the initial length at the folded stable state. On the other hand, the deformation of the prestressed springs behaves differently under the two modes. For the negative mode, the prestressed spring has similar kinematics to the mountain crease. The compressed spring is further shortened while the cell is folding. Then, the spring returns to its initial compressed length at the folded stable state. For the positive mode, the spring is elongated at the initial stable state. As the cell folding initiates, the amount of elongation reduces. At the folded stable state, the spring returns to its initial elongated state. We can see that the deformation history of the prestressed spring in the positive mode and negative mode is quite different. As a result, the two modes lead to distinct shapes of the energy landscape. This observation enriches the programmability of the frustrated cells by means of local crease control. Moreover, we present an additional local frustrated model, i.e., crease rotation, in *SI Appendix*, section 1, Fig. S2, and Table S3.

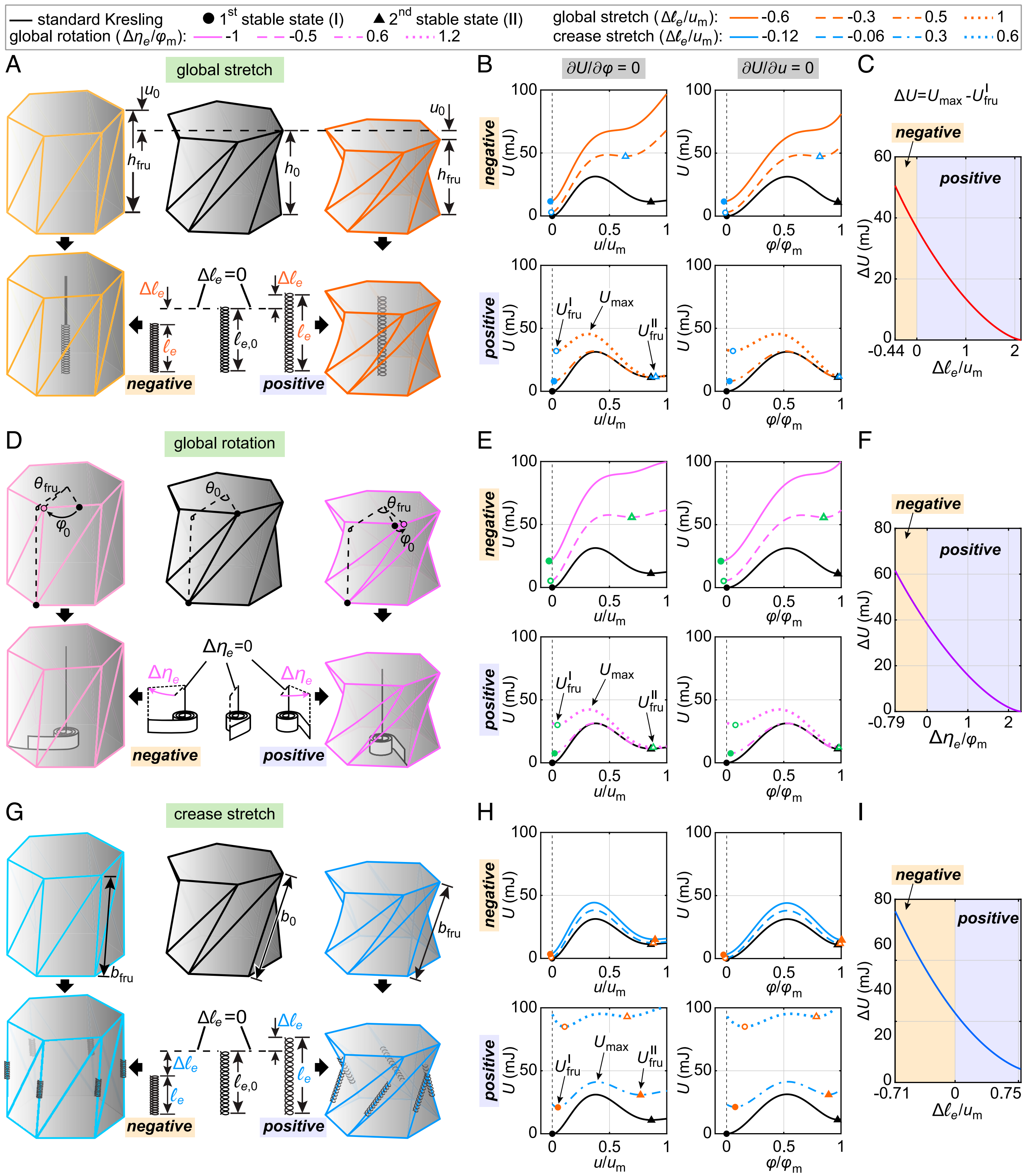

Fig. 2. Theoretical model of geometrically frustrated Kresling origami cells. (*A*) Global stretch feature. Standard Kresling origami (*Top-Middle*) and two frustrated models (*Top-Left* and *Top-Right*). The *Left* model has a compressed spring (negative prestress), while the *Right* one has an extended spring (positive prestress). Here, h_0 denotes the height of the standard Kresling cell, h_{fru} is the height of the frustrated cell, and u_0 is the height difference. (*B*) Reprogrammable energy landscapes. *Top*: intrinsic energy landscape (black) versus tunable landscapes (orange) with the negative prestress model. *Bottom*: intrinsic energy landscape (black) versus tunable landscapes (orange) with the positive prestress model. *Left*: the elastic energy U versus the normalized axial displacement u/u_m under axial loading with free-rotation. *Right*: the elastic energy U versus the normalized twist angle φ/φ_m under torsional loading with free-translation. Notation: u_m denotes maximum displacement, and φ_m maximum twist angle. (*C*) Continuously tunable energy barrier with the global stretch feature. Normalized length changes of the spring $\Delta\ell_e/u_m$ versus the energy barrier ΔU, which is defined as the maximum energy of a frustrated model U_{max} minus the energy at the first stable state U^{I}_{fru}. (*D*) Global rotation feature. Standard Kresling origami (*Top-Middle*) and two frustrated models (*Top-Left* and *Top-Right*). The *Left* model has a deformed torsional spring that rotates the origami clockwise. The *Right* model has a deformed torsional spring that rotates the origami counterclockwise. Here, $\Delta\eta_e$ denotes the rotating angle of the torsional spring. (*E*) Reprogrammable energy landscapes. (*F*) Continuously tunable energy barriers for the frustrated model with global rotation. (*G–I*) Crease (local) stretch feature and the corresponding energy solutions. The symbols b_0 and b_{fru} denote the lengths of mountain creases in the standard and the frustrated model, respectively.

The aforementioned theoretical analysis considers linear spring mechanisms with constant stiffnesses, i.e., $k_{s,e} = constant$ and $k_{r,e} = constant$. However, the theoretical framework (Eqs. **5**–**7**) can be generalized to incorporate nonlinear springs in the frustrated model. We can replace $k_{s,e}$ and $k_{r,e}$ with expressions describing the nonlinear behavior of the spring elements. More details of the theory for nonlinear spring modeling are shown in *SI Appendix*, section 2, Fig. S3, and Table S4.

Experimental Study on Unit Cells. Experiments involve the three frustrated models theoretically investigated in the previous session. We develop a modular fabrication solution to realize the global stretch model, including the spring element, the wire connector, 3D-printed frames, and handles (Fig. 3*A* and Movie S2). The handle controls the level of prestress in the spring element. The spring extension $\Delta\ell$ is a function of the radius of the handle r_{handle} and the number of interval turns n, defined as follows: $\Delta\ell = n(2\pi r_{\mathrm{handle}})/12$. The prestressed spring deforms the standard Kresling into a new equilibrium state configuration. This new stable state is frustrated as it stores elastic energy in both panels and the spring. The amount of energy stored in the frustrated model is tunable by controlling the spring extension. In the compression experiments with the free-rotating fixture, we test three different spring extensions and compare the results with those of the standard origami cell (Movie S2). Fig. 3*B* reports the experimental results and theoretical predictions. For the standard Kresling, we conduct tests on five specimens and calculate the mean value (solid curves) and the corresponding SD (shaded regions) using the formulas in *SI Appendix*, section 3. For the frustrated Kresling, we conduct tests on three specimens for each prestressed model. The error bar at the first stable state is the SD calculated from the measured displacement.

The strain energy plots (Fig. 3 *B*, *Top-Left*) confirm that the frustrated models have nonzero base energy at the initial stable states, and the amount of the base energy depends on the spring extensions. Note that we assume that the spring elements do not contribute to the energy formulation anymore if they are deactivated (i.e., zero prestress). Consequently, the behavior of the frustrated cell becomes identical to that of the standard cell (Fig. 3 *B*, *Bottom-Left*). The plots in Fig. 3*B* (*Right*) illustrate the force–displacement relationship obtained from both experiment and theory, respectively. We zoom in on the initial loading region to show the shift of force curves. Both experimental data and theoretical analysis verify that the starting point of the force curve shifts as the prestress increases. The amount of shift corresponds to the height change at the first stable state in the frustrated models. Note that the magnitude of the peak force decreases as more prestress is applied in experiments. In theoretical analyses, the peak forces are similar. This discrepancy is caused by the panel buckling at initial loading with activated frustration (Fig. 3 *B*, *Bottom-Right*), which is not considered in the theoretical analysis (see more discussion in *SI Appendix*, section 4).

We design a specific mechanism to apply positive prestress in the global rotation model. This mechanism, which behaves like a torsional spring, involves the customized inclined component, the spring element, the wire connector, and 3D-printed frames and handles (Fig. 3*C* and Movie S3). The handle controls the amount of prestress applied along the torsional direction. The torsional angle $\Delta\eta$ and torsional stiffness $k_{r,e}$ are defined as $\Delta\eta = n(2\pi r_{\mathrm{handle}}/r_{\mathrm{frame}})/12$ and $k_{r,e} = T/\Delta\eta$, where T is the reaction torque, and r_{frame} is the radius of the frame. Compared with the standard cell, the prestressed cell is deformed in its initial stable configuration with a nonzero base energy. The elastic energy is stored in both the deformed panels and the spring. Given a constant spring stiffness, the torsional angle controls the magnitude of the energy stored in the initial configuration of the frustrated model. We test three different angles under torsional loading with the free-translating fixture (Movie S3). Both theoretical and experimental results (Fig. 3 *D*, *Left*) verify the capability of the global rotation models for tuning base energy at initial stable states. In addition, the twist angle-torque curves for deactivated and activated frustration are different as shown in Fig. 3 *D* (*Right*). The zoomed-in plots further illustrate the different initial loading points. The shift of those points is related to the amount of prestress applied in the global rotation frustrated models.

The two aforementioned global frustrated models incorporate only positive prestresses. In contrast, the crease (local) stretch with negative prestress further enhances the energy landscape programmability of the frustrated model. The crease stretch prototype involves compressed springs inserted in 3D-printed cases aside from the mountain creases of the cell (Fig. 3*E* and Movie S4). Due to the prestressed spring elements, the frustrated cell gets extended and then stays in a new equilibrium state. The new state has a nonzero elastic base energy contributed by the deformed origami cell and the prestressed spring elements. Tuning the magnitude of the prestress leads to controllable base energy at the initial stable states, as shown in Fig. 3*F* (*Top-Left*). Moreover, the experimental results show that the shape of the energy landscapes depends on prestress levels of the springs. The more the spring element is compressed, the higher energy barrier is achieved for the frustrated cell. This behavior agrees with the theoretical analysis shown in Fig. 3*F* (*Bottom-Left*). Fig. 3*F* (*Right*) verifies that the initial loading positions of samples with deactivated and achieved frustration are different. The initial loading position is related to the configuration of the Kresling origami at the first stable state. The negative displacement u indicates increased height of the origami sample in the frustrated model. On the other hand, we validate the crease (local) stretch with positive prestress. We refer to *SI Appendix*, section 5 and Fig. S4 for more details.

Experimental Study on Assemblies. Beyond the studies at the unit cell level, we explore the mechanical behavior of origami assemblies composed of standard cells and frustrated cells. The cells are modular, and they can be connected by miniature neodymium magnets embedded in the frames.

Standard Kresling assemblies. For an origami array with three standard cells, there are, in total, eight stable states as shown in Fig. 4*A*. In theory, fifty-six folding paths connect any two stable states. In practice, sixteen out of fifty-six folding paths are unachievable without transiting through other stable states (Fig. 4*B*). For instance, state I (with all three cells deployed) cannot deform directly to state VIII (with all three cells folded) unless passing through the other states where one or two cells have been folded. Note that eight additional paths in Fig. 4*C* are infeasible due to the intrinsic energy barrier ΔU built in the three cells, i.e., ΔU(red cell) $>$ ΔU(yellow cell) $\approx$ ΔU(blue cell), which are differentiated by controlling the panel thickness (see details in *Materials and Methods*). Moreover, state VIII cannot be pulled to state V because lower-energy barrier cells (blue or yellow) must deploy before the higher-energy barrier cell (red). As a result, only thirty-two out of fifty-six folding paths are feasible (Fig. 4*D*). Eight feasible paths have been verified experimentally under two types of loading conditions: axial loading and torsional loading (Movie S5, details in Movie S5

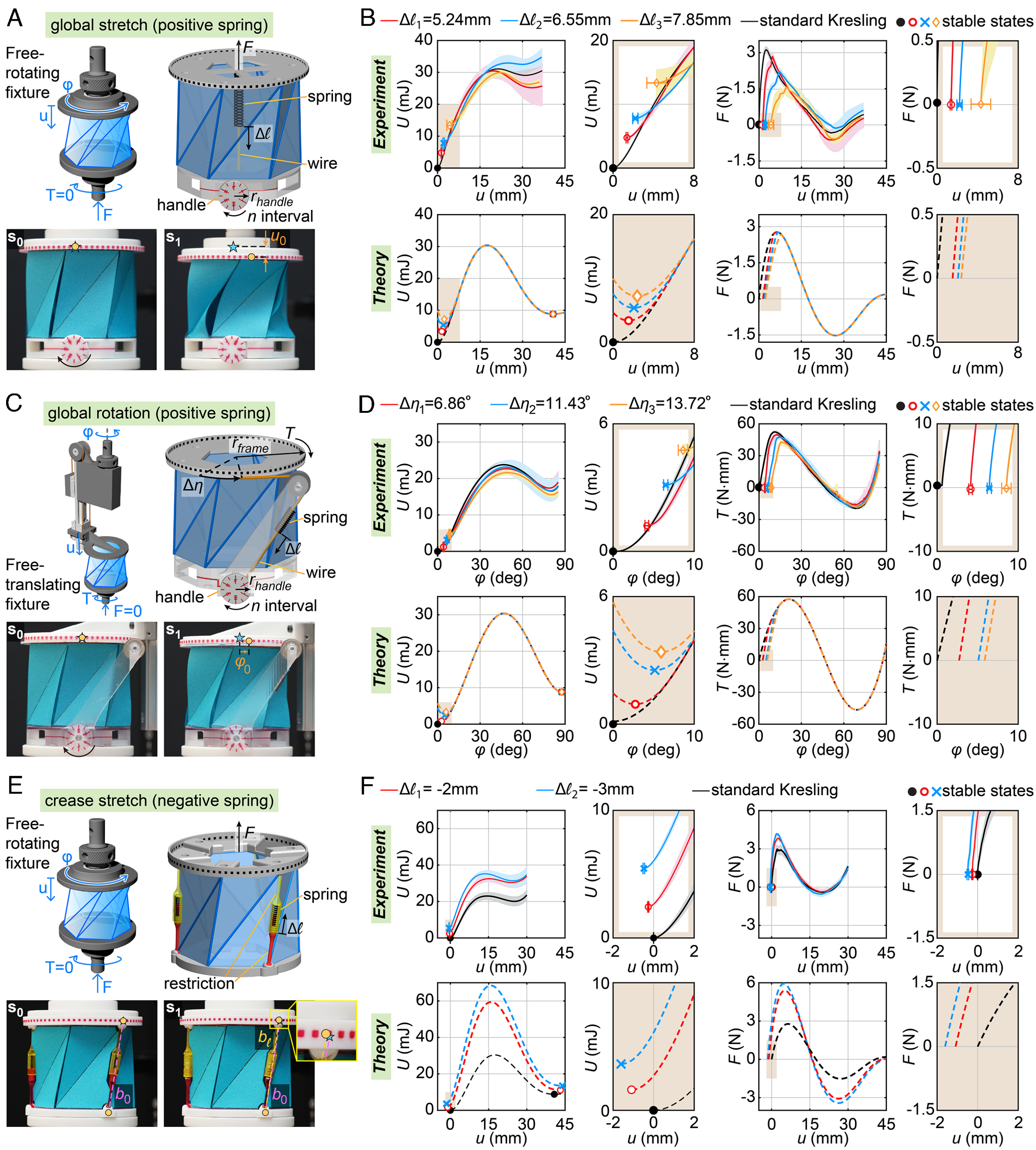

Fig. 3. Experiments involving the three frustrated models of the previous figure. (*A*) Global stretch with positive prestress. *Top-Left*: illustration of axial loading with a free-rotating fixture. *Top-Right*: schematic of the design enabling prestress in the axial direction. *Bottom-Left*: photo of an undeformed origami cell. *Bottom-Right*: photo of a prestressed unit in its initial stable state. (*B*) Experimental results and theoretical predictions. *Top*: experimental results comparing the behavior of the frustrated models with the standard origami cell. Solid lines represent the mean value and shade regions represent the SD of the experimental data. *Bottom*: corresponding theoretical predictions. *Left*: axial displacement u versus stored elastic energy U. *Right*: displacement versus applied force F. The *Insets* highlight the early stages of the test. (*C*) Global rotation with positive prestress. *Top-Left*: illustration of torsional loading with a free-translating fixture. *Top-Right*: schematic of the design with torsional prestress in the cell. *Bottom-Left*: photo of an undeformed origami cell. *Bottom-Right*: photo of a prestressed cell in its initial stable state. (*D*) Experimental results and theoretical predictions. (*E*) Crease (local) stretch with negative prestress. *Top-Left*: illustration of the loading with a free-rotating fixture. *Top-Right*: schematic of the compressed springs strategically located along the mountain creases. *Bottom-Left*: photo of an undeformed origami cell. *Bottom-Right*: photo of a prestressed cell in its initial stable state. (*F*) Experimental results and theoretical predictions.

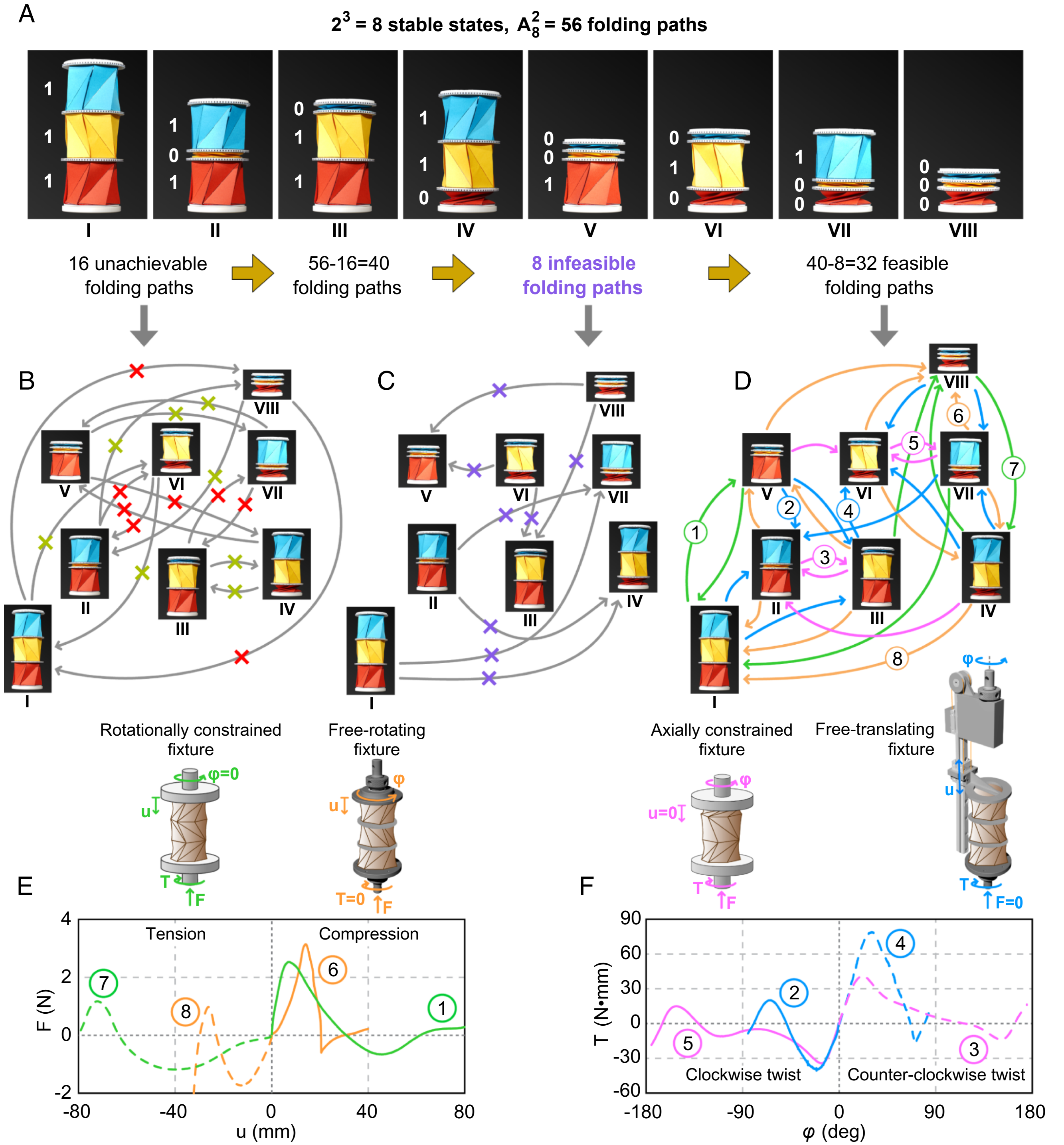

Fig. 4. Deformation paths achieved on 3-cell standard Kresling assembly under four loading conditions. The intrinsic energy barriers (ΔU) have been selected such that ΔU(red cell)>ΔU(yellow cell)≈ΔU(blue cell). The yellow and blue cells have opposite chiralities. (*A*) Stable states. (*B*) Unachievable folding paths. (*C*) Infeasible folding paths. (*D*) Feasible folding paths. (*E*) Experimental results associated to rotationally constrained fixture and free-rotating fixture. The circled numbers in the plot correspond to those in panel (*D*). (*F*) Experimental results associated to axially constrained fixture and free-translating fixture. The circled numbers in the plot correspond to those in panel (*D*).

are shown in *SI Appendix*, section 6 and Fig. S5). The axial loading condition involves two fixtures, i.e., one is rotationally constrained, and the other one displays free rotation (see more details in *SI Appendix*, section 7). The corresponding testing results are presented in Fig. 4*E*. On the other hand, the torsional loading condition is equipped with the axially constrained fixture and the free-translating fixture, respectively. The corresponding experimental data are shown in Fig. 4*F*. According to the experimental data, we calculate the energy landscapes of eight feasible paths in *SI Appendix*, section 8 and Fig. S6.

Frustrated Kresling assemblies. The 3-cell origami assembly shown in Fig. 5*A* is prestressed such that the *Top* two cells include springs on the mountain creases (local level) and the *Bottom* cell includes a rotational spring (global level). Each of the frustrated

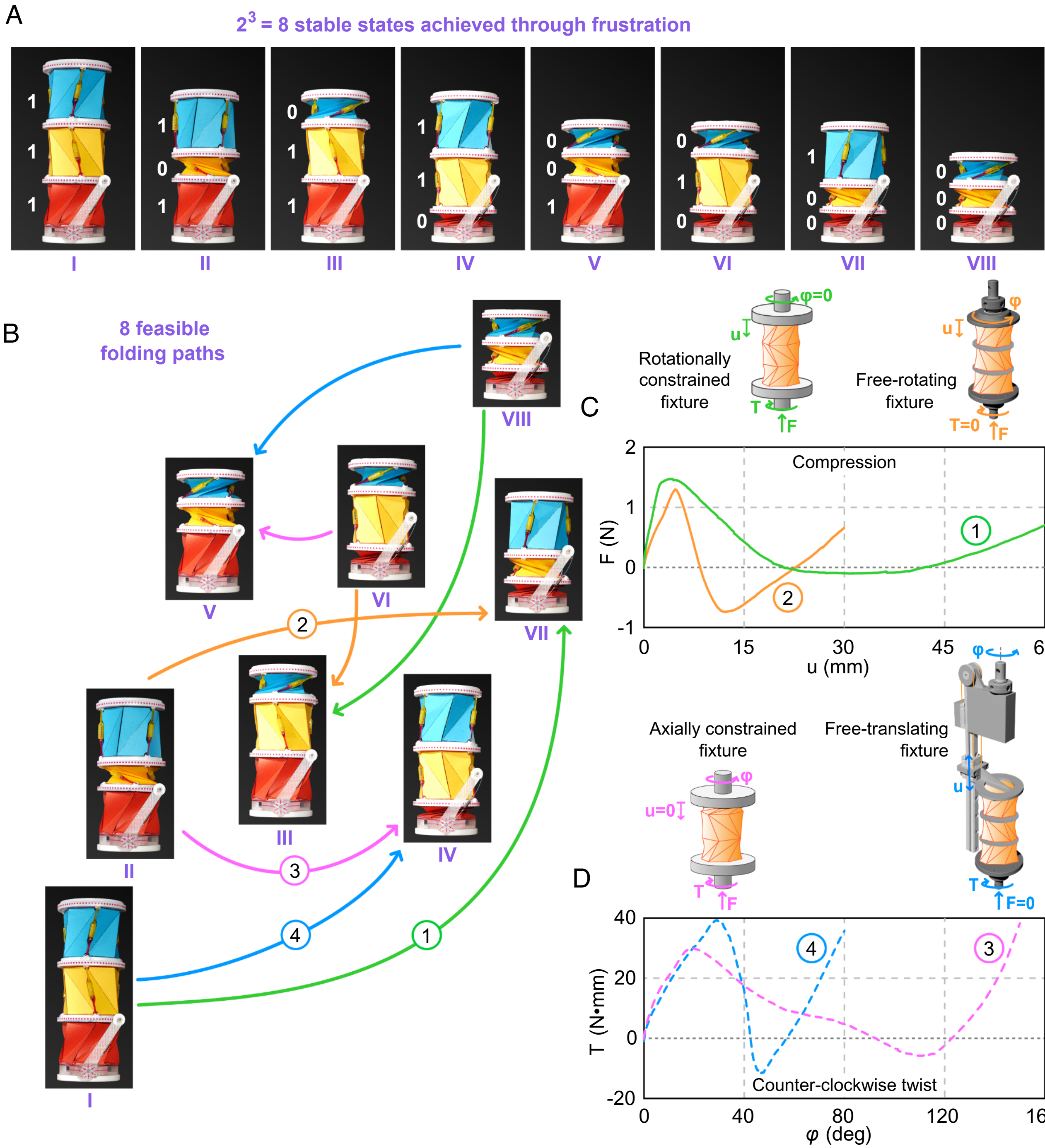

Fig. 5. Deformation paths achieved on 3-cell frustrated Kresling assembly under four loading conditions. The energy barriers of the frustrated cells (ΔU_{fru}) have been controlled such that ΔU_{fru}(red cell) < ΔU_{fru}(yellow cell) ≈ ΔU_{fru}(blue cell). The yellow and blue cells have opposite chiralities. (*A*) Stable states. (*B*) Feasible folding paths, which were infeasible in the previous figure. (*C*) Experimental results associated to rotationally constrained fixture and free-rotating fixture. The circled numbers in the plot correspond to those in panel (*B*). (*D*) Experimental results associated to axially constrained fixture and free-translating fixture. The circled numbers in the plot correspond to those in panel (*B*). The experimental result of path ④ is the same as displayed in Fig. 1.

cells has two stable states with tunable energy barriers enabled by the prestressing level. As a result, the assembly has, in total, eight stable states, like Fig. 4; however, the behavior is quite different. The frustrated assembly can be continuously reprogrammed by means of local cell control. This reprogrammability leads to precise control of the folding sequences, and enables the eight previously infeasible folding paths of Fig. 4*C* to be achieved as feasible folding paths in Fig. 5*B*. For example, although the intrinsic energy barrier of the red cell is bigger than that of the blue cell, the global rotation mechanism actively lowers the red cell energy barrier. Therefore, when state I deforms to state VII following path ①, the frustrated red cell folds while the blue cell remains deployed during the process. The loading condition for this deformation is axial compression with a rotationally constrained fixture, as shown by the green curve in Fig. 5*C* (Movie S6). The plot has an orange curve, which corresponds to the feasible deformation path ② in Fig. 5*B*, under axial loading with free-rotating fixture (Movie S6). Other

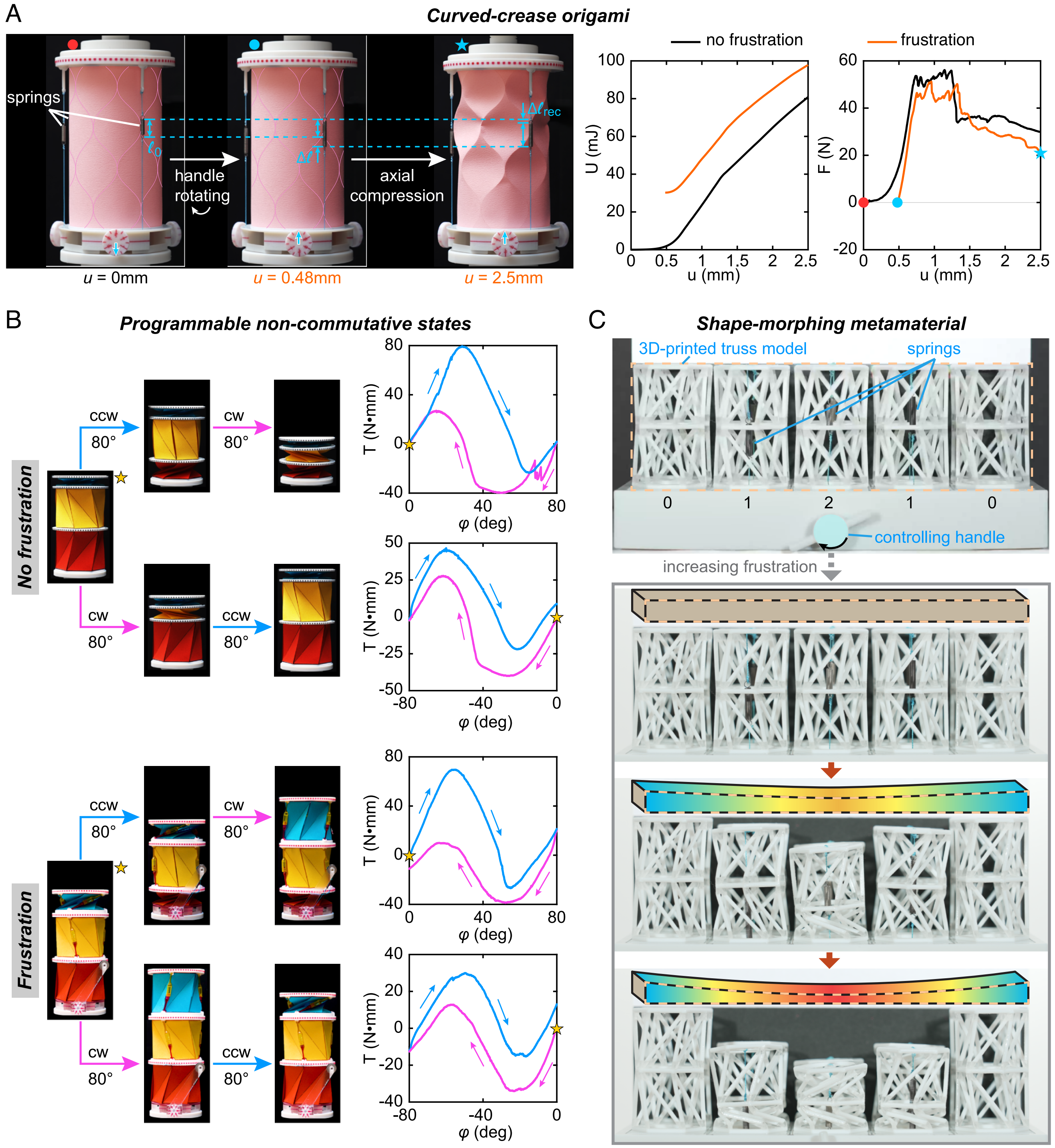

Fig. 6. Scope of frustration. (*A*) Frustrated curved-crease origami structure. *Left*: photos of the nonfrustrated curved-crease origami, the frustrated curved-crease origami, and the buckled curved-crease origami, respectively. *Right*: experimental data of nonfrustrated and frustrated curved-crease origami structures. (*B*) Programmable noncommutative states enabled by frustration. *Top*: folding paths and corresponding twist angle versus torque curves for the nonfrustrated Kresling array. *Bottom*: folding paths and corresponding twist angle versus torque curves for the frustrated Kresling array. ccw, counterclockwise twist; cw, clockwise twist. (*C*) Shape-morphing metamaterial with controllable frustration. *Top*: 3D-printed truss model embedded with different springs. The stiffness of the springs in column 1 and column 2 is 0.11 N/mm and 0.35 N/mm, respectively. *Bottom*: deformed configurations for different amounts of prestress applied in the springs.

feasible folding paths, i.e., path ③ and path ④, are achieved by torsional loading conditions with the axially constrained fixture and the free-translating fixture, respectively, as shown in Fig. 5*D* (Movie S6). In addition, energy landscapes corresponding to feasible paths in Fig. 5 *C* and *D* are presented in *SI Appendix*, section 8 and Fig. S7. More details of the reprogrammability of the feasible folding paths and energy landscapes are shown in *SI Appendix*, section 9 and Fig. S8.

The results in Fig. 5 demonstrate that the ability to switch among different states, by controlling the prestressing levels, enables the eight feasible folding paths of Fig. 5*B*, something not achievable with the nonfrustrated Kresling array (Fig. 4). While these folding paths could also be enabled by designing new cells with predefined energy barriers, through material and/or geometry selections, this discrete approach inevitably introduces new infeasible folding paths and does not support in-situ reconfiguration. In contrast, the continuous approach of geometric frustration, combined with a finely tuned spring mechanism, enables the elimination of infeasible folding paths. This allows for dynamic reprogramming of folding behavior within the same array, leading to adaptability and control.

Scope of Frustration. Though our designs of frustration are created based on Kresling origami structure, they can be used to embed frustration into other origami structures. For instance, Fig. 6*A* gives an example to explore the influence of prestressing on a curved-crease origami tube. The states at the red and blue points as well as the force curves indicate that the mechanism with stretching spring causes a shift of initial state of the origami tube. Under axial compression loading, the frustrated curved-crease tube exhibits significant panel buckling (see the state at the blue-star point in Fig. 6*A*). Moreover, detailed comparison between the frustrated and nonfrustrated curved-crease origami is shown in *SI Appendix*, section 10 and Fig. S9.

The second application relates to programmable noncommutative behavior of Kresling arrays (Fig. 6*B*). We consider a Kresling array consisting of two lower energy barrier cells at the top and one higher energy barrier cell at the bottom, and consider two examples, one that does not involve frustration and one that does. In both examples, we apply counterclockwise twist followed by clockwise twist, and then we reverse the actuation sequence (i.e., clockwise twist followed by counterclockwise twist), always resulting in a total zero net twist at the end of each actuation sequence. For the first example, the array shows history-dependent behavior in the sense that the deformed configuration depends on the sequence of the twist actuation. We demonstrate this feature by experiments on a reference configuration under the actuation sequences described above (Fig. 6 *B*, *Top*). Note that details of the jagged portion on the unloading curve are elaborated in *SI Appendix*, section 11 and Fig. S10. The two different end configurations demonstrate the relevance of twisting history, which indicates noncommutative behavior. For the example involving frustration, the top unit cell (blue) is the same as before; however, the bottom two cells are frustrated. The middle cell has linear (local) springs (with induced negative prestress) providing it with a higher energy barrier than the top cell. The bottom cell has an especially designed torsional (global) spring (with induced positive prestress) providing it with the highest energy barrier of the assembly. We observe noncommutative state transitions as well (Fig. 6 *B*, *Bottom*); however, comparatively, the two final states in the frustrated Kresling array are different from those in the nonfrustrated Kresling array, resulting in a programmable (frustration-dependent) noncommutative state transition.

Furthermore, we create a shape-morphing metamaterial by embedding the spring mechanism into a 3D-printed truss prototype involving multiple Kresling columns (43) (Fig. 6*C*). The level of prestress in each Kresling column depends on the stiffness of springs. Here, column 0 has no spring, while the stiffness of the springs in column 1 and column 2 is 0.11 N/mm and 0.35 N/mm, respectively. All the springs are connected with a handle through wires. Rotating the handle applies a constant stretch to all the springs. Since the spring of column 2 has the highest stiffness, it deforms more than column 1 and column 0 (Fig. 6 *C*, *Bottom*). As a result, the varying deformation in different columns allows the metamaterial to achieve shape-morphing behavior.

Discussion

We present geometrically frustrated Kresling assemblies with tunable energy landscapes and folding paths. The assembly is modular, and it consists of both standard origami cells and frustrated cells. We introduce frustrated modules with three types of prestress, i.e., global stretch, global rotation, and crease (local) stretch. The prestress of the frustrated model is continuously adjustable by controlling the special springs, which allows for changing the energy barrier for the cell. The theoretical analysis verifies that the energy landscape for the frustrated cells is programmable and the corresponding energy barrier is continuously tunable. We prototype all three types of frustrated origami cells and use four loading and boundary conditions to validate the behavior of the cells experimentally. Experiments demonstrate that activating and deactivating frustration can dramatically enhance the programmability of the origami assembly, unlocking otherwise infeasible folding paths. The present concept can be implemented widely in reconfigurable systems where in-situ programmability is needed in the application, e.g., adaptable metamaterials for shape morphing.

Materials and Methods

Formulation of the Frustration Theory. Since the frustrated cell can be controlled by both axial force, F, and torque, T, the work done on the cell is calculated by $W(u,\varphi) = \int F du + \int T d\varphi$. The total potential energy of the frustrated cell, Π, can be expressed using the total elastic energy, U_{fru}, and work, W, i.e.,

$$\Pi(u,\varphi) = U_{\mathrm{fru}}(u,\varphi) - W(u,\varphi). \quad [8]$$

Notice that $\Pi(u,\varphi)$ is a function of two independent variables, u and φ. Based on the principle of minimum total potential energy, equilibrium is achieved when $\partial\Pi/\partial u = 0$ and $\partial\Pi/\partial\varphi = 0$. Thus, the axial force, F, and the torque, T, are calculated by

$$F(u,\varphi) = \frac{\partial U_{\mathrm{fru}}(u,\varphi)}{\partial u},\ T(u,\varphi) = \frac{\partial U_{\mathrm{fru}}(u,\varphi)}{\partial \varphi}. \quad [9]$$

Fabrication of Kresling Origami Cells. Both standard and frustrated origami cells were fabricated by a material composed of multilayer origami papers (Tant) and adhesive tapes in between (3M 9474LE, 0.17mm-thick). The crease patterns of the blue and yellow cells include two layers of origami papers and one layer of adhesive tape. The crease pattern of the red cell is made of three layers of origami papers and two layers of adhesive tapes. We cut the mountain creases for all the cells. Additionally, for the crease (local) stretch (Fig. 3*E*) design, we cut a trapezoid hole on the panel to avoid interaction between the prestressed element and the origami cell. More details are shown in *SI Appendix*, section 12 and Fig. S11.

Fabrication of 3D-Printed Truss. The 3D-printed truss model in Fig. 6*C* consists of two components: rods and soft joints, which are fabricated using a Stratasys J55 Prime polyjet printer. The rods are printed using the VeroWhite material, and the joints are printed using FLXA9950 (Shore-A 50), with a mix of VeroUltraClear and ElasticoClear.

Fabrication of Prestressed Elements. The 3D printed prestressed components are fabricated using a Stratasys J55 Prime polyjet printer. For the global stretch model, the frames and handle are printed by the VeroWhite material, and the markers are printed by the VeroMagenta material. For the global rotation model, the top frame and markers are fabricated by the same material as the global stretch design, while the bottom frame and handle are printed by the VeroUltraClear material. For the crease (local) stretch model, the frames and markers are printed by the same material as the global stretch one, while the case assembled on the top and bottom frames printed by the VeroYellow and VeroMagenta materials,respectively. The pulley used in the global rotation model is a ball bearing pulley (MiSUMi, SZV3-12). The spring used in the global stretch model is an extension spring (McMaster-Carr, 9065K566). The spring used in the global rotation model is an extension spring (McMaster-Carr, 5108N036). The spring used in the crease (local) stretch model is a compression spring (McMaster-Carr, 9657K641). The springs in the global models are connected to the 3D-printed components using a 0.3 mm diameter fishing wire. More detailed parameters are provided in *SI Appendix*, section 12. Note that the spring system can be manufactured by standard 3D printers, which enhances the practicality of the frustration concept. For instance, we show an illustration of integrating 3D-printed springs into cell origami in *SI Appendix*, section 12 and Fig. S12.

Experimental Setups. In Fig. 3, we conduct both compression tests and torsion tests on an Instron loading frame machine (Model 68SC-5 Single Column Testing System), equipped with free-rotating and free-translating fixtures, respectively (see more information in *SI Appendix*, section 12 and Fig. S13). The applied axial load and torque have been measured with a force/torque sensor (Biaxial Load Cell $\pm$445 N, $\pm$5.65 Nm). The compression experiments are conducted at a speed of 0.25 mm/s, while the torsional experiments are performed at 0.5 deg/s. In Figs. 4 and 5, we conduct compression tests using both rotationally constrained and free-rotating fixtures. Moreover, we conduct torsion tests using both axially constrained and free-translating fixtures.

Data, Materials, and Software Availability. All study data are included in the article and/or supporting information.

ACKNOWLEDGMENTS. This research was supported by Margareta E. Augustine Professorship of Engineering at Princeton University and the NSF under grant no. 2323276. D.M. acknowledges financial support from the European Union, European Research Council grant HE GA 101086644 S-FOAM (Views and opinions expressed are however those of the author(s) only and do not necessarily reflect those of the European Union or the European Research Council Executive Agency. Neither the European Union nor the granting authority can be held responsible for them).

Author affiliations: [a]Department of Civil and Environmental Engineering, Princeton University, Princeton, NJ 08544; [b]Department of Civil, Environmental and Mechanical Engineering, University of Trento, Trento 38122, Italy; and [c]Princeton Materials Institute, Princeton University, Princeton, NJ 08544

Author contributions: S.Z., T.Z., D.M., and G.H.P. designed research; S.Z., T.Z., D.M., and G.H.P. performed research; S.Z., T.Z., and D.M. contributed new reagents/analytic tools; S.Z., T.Z., D.M., and G.H.P. analyzed data; and S.Z., T.Z., D.M., and G.H.P. wrote the paper.

1. S. Shan *et al.*, Multistable architected materials for trapping elastic strain energy. *Adv. Mater.* **27**, 4296–4301 (2015).
2. T. Chen, J. Mueller, K. Shea, Integrated design and simulation of tunable, multi-state structures fabricated monolithically with multi-material 3d printing. *Sci. Rep.* **7**, 45671 (2017).
3. K. Bertoldi, P. M. Reis, S. Willshaw, T. Mullin, Negative Poisson's ratio behavior induced by an elastic instability. *Adv. Mater.* **22**, 361–366 (2010).
4. S. H. Kang *et al.*, Complex ordered patterns in mechanical instability induced geometrically frustrated triangular cellular structures. *Phys. Rev. Lett.* **112**, 098701 (2014).
5. A. Rafsanjani, A. Akbarzadeh, D. Pasini, Snapping mechanical metamaterials under tension. *Adv. Mater.* **27**, 5931–5935 (2015).
6. W. Li, F. Wang, O. Sigmund, X. S. Zhang, Digital synthesis of free-form multimaterial structures for realization of arbitrary programmed mechanical responses. *Proc. Natl. Acad. Sci. U.S.A.* **119**, e2120563119 (2022).
7. T. Chen, O. R. Bilal, K. Shea, C. Daraio, Harnessing bistability for directional propulsion of soft, untethered robots. *Proc. Natl. Acad. Sci. U.S.A.* **115**, 5698–5702 (2018).
8. A. Rafsanjani, K. Bertoldi, A. R. Studart, Programming soft robots with flexible mechanical metamaterials. *Sci. Robot.* **4**, eaav7874 (2019).
9. X. Guo, M. Guzmán, D. Carpentier, D. Bartolo, C. Coulais, Non-orientable order and non-commutative response in frustrated metamaterials. *Nature* **618**, 506–512 (2023).
10. A. Pal, M. Sitti, Programmable mechanical devices through magnetically tunable bistable elements. *Proc. Natl. Acad. Sci. U.S.A.* **120**, e2212489120 (2023).
11. P. Wang, F. Casadei, S. Shan, J. C. Weaver, K. Bertoldi, Harnessing buckling to design tunable locally resonant acoustic metamaterials. *Phys. Rev. Lett.* **113**, 014301 (2014).
12. P. Jiao, J. Mueller, J. R. Raney, X. Zheng, A. H. Alavi, Mechanical metamaterials and beyond. *Nat. Commun.* **14**, 6004 (2023).
13. J. T. Overvelde, S. Shan, K. Bertoldi, Compaction through buckling in 2D periodic, soft and porous structures: Effect of pore shape. *Adv. Mater.* **24**, 2337–2342 (2012).
14. K. Bertoldi, V. Vitelli, J. Christensen, M. Van Hecke, Flexible mechanical metamaterials. *Nat. Rev. Mater.* **2**, 1–11 (2017).
15. B. Kresling, "Natural twist buckling in shells: From the hawkmoth's bellows to the deployable Kresling-pattern and cylindrical Miura-Ori (2008)" in *Proceedings of the 6th International Conference on Computation of Shell and Spatial Structures IASS-IACM: "Spanning Nano to Mega"*, J. F. Abel, J. R. Cooke, Eds. (Cornell University, Ithaca, NY, 2008), pp. 18–21.
16. H. Yasuda, T. Tachi, M. Lee, J. Yang, Origami-based tunable truss structures for non-volatile mechanical memory operation. *Nat. Commun.* **8**, 1–7 (2017).
17. K. Liu, G. H. Paulino, Nonlinear mechanics of non-rigid origami: An efficient computational approach. *Proc. R. Soc. A Math. Phys. Eng. Sci.* **473**, 20170348 (2017).
18. Z. Zhai, Y. Wang, H. Jiang, Origami-inspired, on-demand deployable and collapsible mechanical metamaterials with tunable stiffness. *Proc. Natl. Acad. Sci. U.S.A.* **115**, 2032–2037 (2018).
19. H. Yasuda *et al.*, Origami-based impact mitigation via rarefaction solitary wave creation. *Sci. Adv.* **5**, eaau2835 (2019).
20. S. Wu, T. Zhao, Y. Zhu, G. H. Paulino, Modular multi-degree-of-freedom soft origami robots with reprogrammable electrothermal actuation. *Proc. Natl. Acad. Sci. U.S.A.* **121**, e2322625121 (2024).
21. J. L. Silverberg *et al.*, Origami structures with a critical transition to bistability arising from hidden degrees of freedom. *Nat. Mater.* **14**, 389–393 (2015).
22. J. Ma, S. Zang, Y. Chen, Z. You, The tessellation rule and properties programming of origami metasheets built with a mixture of rigid and non-rigid square-twist patterns. *Engineering* **17**, 82–92 (2022).
23. B. H. Hanna, J. M. Lund, R. J. Lang, S. P. Magleby, L. L. Howell, Waterbomb base: A symmetric single-vertex bistable origami mechanism. *Smart Mater. Struct.* **23**, 094009 (2014).
24. F. Lechenault, M. Adda-Bedia, Generic bistability in creased conical surfaces. *Phys. Rev. Lett.* **115**, 235501 (2015).
25. H. Yasuda, J. Yang, Reentrant origami-based metamaterials with negative Poisson's ratio and bistability. *Phys. Rev. Lett.* **114**, 185502 (2015).
26. S. Li, K. Wang, Fluidic origami with embedded pressure dependent multi-stability: A plant inspired innovation. *J. R. Soc. Interface* **12**, 20150639 (2015).
27. Y. Li, S. Pellegrino, A theory for the design of multi-stable morphing structures. *J. Mech. Phys. Solids* **136**, 103772 (2020).
28. N. P. Bende *et al.*, Geometrically controlled snapping transitions in shells with curved creases. *Proc. Natl. Acad. Sci. U.S.A.* **112**, 11175–11180 (2015).
29. T. U. Lee *et al.*, Self-locking and stiffening deployable tubular structures. *Proc. Natl. Acad. Sci. U.S.A.* **121**, e2409062121 (2024).
30. D. Misseroni *et al.*, Origami engineering. *Nat. Rev. Methods Prim.* **4**, 40 (2024).
31. D. Melancon, B. Gorissen, C. J. García-Mora, C. Hoberman, K. Bertoldi, Multistable inflatable origami structures at the metre scale. *Nature* **592**, 545–550 (2021).
32. X. Zhang *et al.*, Kirigami-based metastructures with programmable multistability. *Proc. Natl. Acad. Sci. U.S.A.* **119**, e2117649119 (2022).
33. K. Liu, P. P. Pratapa, D. Misseroni, T. Tachi, G. H. Paulino, Triclinic metamaterials by tristable origami with reprogrammable frustration. *Adv. Mater.* **34**, 2107998 (2022).
34. R. Rodriguez-Feliciano, K. Wang, Synthesis of a highly programmable multistable kresling origami-inspired unit cell. *Int. J. Mech. Sci.* **284**, 109768 (2024).
35. M. Mirkhalaf, A. Rafsanjani, Harnessing machine mechanisms to continuously reprogram metamaterials. *Matter* **6**, 3719–3731 (2023).
36. T. Chen, M. Pauly, P. M. Reis, A reprogrammable mechanical metamaterial with stable memory. *Nature* **589**, 386–390 (2021).
37. X. Fang *et al.*, Programmable gear-based mechanical metamaterials. *Nat. Mater.* **21**, 869–876 (2022).
38. L. A. Shaw, S. Chizari, M. Dotson, Y. Song, J. B. Hopkins, Compliant rolling-contact architected materials for shape reconfigurability. *Nat. Commun.* **9**, 4594 (2018).
39. Y. Zhang, M. Velay-Lizancos, D. Restrepo, N. D. Mankame, P. D. Zavattieri, Architected material analogs for shape memory alloys. *Matter* **4**, 1990–2012 (2021).
40. L. Wu, D. Pasini, In situ activation of snap-through instability in multi-response metamaterials through multistable topological transformation. *Adv. Mater.* **35**, 2301109 (2023).
41. J. F. Sadoc, R. Mosseri, *Geometrical Frustration* (Cambridge University Press, 1999).
42. S. Zang, D. Misseroni, T. Zhao, G. H. Paulino, Kresling origami mechanics explained: Experiments and theory. *J. Mech. Phys. Solids* **188**, 105630 (2024).
43. T. Zhao *et al.*, Modular chiral origami metamaterials. *Nature* **640**, 931–940 (2025).